

PAPER

View Article Online
View Journal | View Issue

Cite this: *Biomater. Sci.*, 2024, **12**, 1914

Application of a meshed artificial dermal scaffold and negative-pressure wound therapy in the treatment of full-thickness skin defects: a prospective *in vivo* study

Pei Wei, ^{†a,b,c} Lijiao Wu, ^{†d,e} Hongteng Xie, ^{a,b,c} Zhaohong Chen,^{a,b,c} Rongwei Tan^f and Zhaorong Xu ^{*a,b,c}

Artificial dermal scaffolds (ADSs) have great value in repairing deep skin defects. However, problems such as unsatisfactory angiogenesis and local dropsy or empyema often occur, resulting in delayed or even failed wound healing. Negative pressure wound therapy (NPWT) is an effective therapy to promote wound healing or shorten wound bed preparation time. Studies on whether it can improve the effects of ADSs have never been interrupted, and no consensus has been reached. In this study, an improved ADS was prepared by mesh technology, physicochemical experiments were conducted, cell adhesion and proliferation were assessed with the meshed ADS, and *in vivo* experiments were conducted to investigate the effects of meshed ADS or ADS combined with NPWT in repairing full-thickness skin defects. The results showed that the meshed ADS showed through-layer channels arranged in parallel longitudinal and transverse intersections. The cell experiments confirmed the good cytocompatibility. The *in vivo* experiments showed that there were no differences in the take rate or contraction of grafted skin among all experiment groups. The meshed ADS exhibited good histocompatibility, and there were no differences in tissue inflammation, dermal angiogenesis, or degradation among all groups. In addition, necrosis, dropsy, or empyema of the dermal scaffold were found in all experiment groups except for the meshed ADS + NPWT group, which showed better wound repair results, including fewer scaffold-related complications and satisfactory skin graft survival and wound contraction. In conclusion, this novel meshed ADS, which has a regular through-layer mesh structure and possesses stable physicochemical properties and good biocompatibility, combined with NPWT can ensure adequate subdermal drainage and reduce the risk of scaffold-related complications, thereby improving the quality and efficiency of wound repair, promoting a broader application of biomaterials, and helping physicians and readers implement more effective wound management.

Received 15th October 2023,
Accepted 20th December 2023

DOI: 10.1039/d3bm01675g

rsc.li/biomaterials-science

Introduction

Skin acts as an important protective barrier to maintain homeostasis against pathogens, regulate body temperature, and provide sensation and endocrine function.¹ A superficial

skin injury can be repaired by the proliferation, differentiation, and migration of stem cells located in the epidermal basal layer or adnexal structures. However, for deep skin and subcutaneous tissue defects, the damaged areas cannot be restored to their original structure and function by themselves. Autologous split-thickness skin or flap transplantation is needed, but the secondary damage it causes to the donor site and the body itself cannot be underestimated.^{2,3} With the emergence of artificial dermal scaffolds (ADSs), many scholars began to use ADSs combined with split-thickness skin grafts for deep wound repair.⁴

In contrast with natural dermal scaffolds, most ADSs have a bilayer structure that mimics normal skin structure. The upper layer is a semipermeable medical silicone film that simulates the epidermis layer and resists water evaporation and microbial invasion. The lower layer simulates the spongy dermis, which comprises collagen, other biological materials, or synthetic

^aBurn and Wound Repair Department, Fujian Medical University Union Hospital, Fuzhou 350001, China. E-mail: 234828306@qq.com; Tel: +86-059183357896

^bFujian Burn Institute, Fujian Medical University Union Hospital, Fuzhou 350001, China

^cFujian Provincial Key Laboratory of Burn and Trauma, Fujian Medical University Union Hospital, Fuzhou 350001, China

^dDepartment of Orthopedic Surgery, Fujian Provincial Hospital South Branch, Fuzhou 350001, China

^eShengli Clinical Medical College, Fujian Medical University, Fuzhou 350001, China

^fGuangDong Engineering Technology Research Center of Implantable Medical Polymer, Shenzhen Lando Biomaterials Co., Ltd., Shenzhen 518107, China

[†]These authors contributed equally to this study.


polymers and has good biocompatibility and low immunogenicity.^{5,6} For deep wound repair, the ADS dermis, as a template for dermal regeneration, can effectively guide dermal regeneration and optimize the elasticity, flexibility, and mechanical resistance of the healing area.⁷ Currently, ADSs not only provide a new choice for deep wound repair but have also been widely used in burn and plastic surgery,⁸ oral and maxillofacial surgery,⁹ and abdominal surgery.¹⁰ Although the ADS performs well in various fields, the unsatisfactory dermal angiogenesis and the risk of infection should not be ignored.^{11,12} These problems may lead to the failure of tissue repair and other concerns.^{13,14} Therefore, novel ADSs have been developed with the aim of improving their composition and structure or combining them with other technologies to optimize the speed of dermal angiogenesis and reduce the occurrence of certain complications, thus improving their clinical effects.¹⁵

Negative pressure wound therapy (NPWT) creates a closed area of negative pressure around the wound using a negative pressure drainage device. NPWT has the obvious advantages of creating a moist healing environment, shrinking the wound margin, removing necrotic and undesirable secretions, relieving tissue oedema, and reducing dressing change frequency.¹⁶ Therefore, since the 1990s, NPWT has been widely used as a simple and effective adjuvant technique in the management of complex chronic or acute wounds to promote wound repair or shorten the wound bed preparation time. NPWT could stimulate the release of local cytokines through mechanical stress and the hypoxic environment, which not only increases the amount of microangiogenesis in the early stage of wound healing but also promotes the structural stability and maturation of wound microvessels in the later stage.^{17,18} As a result, there has been an increasing number of studies on the application of ADSs combined with NPWT in acute and chronic wounds. It has been reported that NPWT combined with ADS could create a better attachment of the ADS to the wound by reducing the movement between the ADS and the basal layer and enhancing the local nutrient supply to the ADS dermis, which accelerates angiogenesis and mitigates the rates of infection.^{19,20} However, other studies have shown that NPWT has no significant effect on ADS dermal angiogenesis, the take rate of grafted skin, or other long-term effects.^{21,22} The results of these studies are not uniform and do not provide guidance for clinical practice. Therefore, it remains to be seen whether NPWT combined with ADS can improve angiogenesis in the ADS dermis, reduce the occurrence of complications, and improve the quality of wound repair.

In this study, a bilayer ADS with an upper silicone layer and a lower three-dimensional, porous, collagen-based layer was selected, and it was prepared with an improved vertical network structure and an increased longitudinal channel. Using both *in vivo* and *in vitro* experiments, we further explored the physicochemical properties and therapeutic effects of the improved ADS alone and combined with NPWT to repair full-thickness skin defects to find the optimal ADS structure and working pattern.

Experimental

Materials

The meshed ADS used in our study is based on the commercialized Lando® Artificial Dermal Regeneration Matrix, an ADS that has a double-layer structure. The upper layer is a semi-permeable medical silicone membrane, which has a water vapor transmission rate that is similar to that of normal human skin. The lower layer is a cross-linked collagen-chondroitin sulfate dermal scaffold. The preparation details of the meshed ADS are described below. Collagenase (125 U mg⁻¹, Sigma-Aldrich) was used for the *in vitro* degradation test. Mouse fibroblast cells (L929) and human umbilical vein endothelial cells (HUVECs) were used for cytological evaluation. Bama miniature pigs were used for the *in vivo* investigations.

Preparation of meshed ADS

The ADS was placed on the carrier and processed by the specific mesh machine (MT-5, China), which utilized a roller device with staggered cuts. The prepared channels throughout the whole layer were 2 mm long and 1.5 mm apart and regularly arranged in parallel longitudinal and transverse intersections with a network appearance.

Characterization

Micromorphology. The meshed ADS and ADS were cleaned and dehydrated with 50%, 70%, 90%, and 100% ethanol in succession. Next, the ADSs were dried in a freeze-dryer and coated with a thin layer of gold. The surface and cross-sections of the microstructures were observed using a HITACHI TM3030 scanning electron microscope (SEM).

Porosity. The porosity value of the dermal scaffolds was evaluated according to previous reports.²³ Briefly, each sample was immersed in a glass bottle filled with ethanol and removed after it was fully impregnated with ethanol. The weight of the glass bottle filled with ethanol was recorded as *W*₁, and that of the glass bottle containing ethanol and the immersed sample was recorded as *W*₂. After removing the sample, the weight of the bottle with ethanol was defined as *W*₃. Finally, the weight of each dried sample was recorded as *W*_S. The porosity of the sample was calculated as $(W_2 - W_3 - W_S)/(W_1 - W_3) \times 100\%$.

Tensile strength. The silicone layer of the meshed ADS or ADS was cut into a size of 20 mm × 20 mm. The test was conducted as follows: one end of the sample was fixed, and the other was allowed to hang naturally and fixed to a clamp that could be moved vertically. Then, the clamp was moved at a speed of 100 ± 10 mm min⁻¹ until the silicone membrane was torn. The maximum force that the silicone membrane could withstand was recorded as the tensile strength.

Enzymatic degradation. After freeze-drying, the samples were cut into 20 mm × 10 mm pieces and placed in a 15 ml EP tube with 4 ml of 50 U ml⁻¹ collagenase. At different time intervals (5 h, 10 h, 24 h), 2 ml of degradation solution was taken from each tube and placed in a 25 ml glass bottle (stored at 4 °C). At the end of sampling, 2 ml of 12 M HCl was added to each tube, and the remaining sample was completely



degraded in a water bath at 60 °C for 30 min. Then, 2 ml of degradation solution was placed in a 25 ml glass bottle. Next, 2 ml of 12 M HCl was added to the degradation solution collected above, followed by acid hydrolysis at 110 °C in a ventilated drying oven for 24 h. After cooling, 20 µl phenolphthalein indicator and 6 M NaOH were used to neutralize the acid hydrolysis solution. Then, the hydrolysis solution was titrated to 25 ml with water. Finally, the absorbance of the degradation solution at 560 nm was measured, and the degradation rate was calculated.

Cytocompatibility

HUVECs and L929 cells were seeded on the dermal scaffold at a density of 105 cells per ml in 48-well plates. The culture medium was changed every other day. On days 1, 4, 7, and 14, the dermal scaffolds were removed from the culture system, washed twice with PBS, and divided into two parts. One part was then fixed with formaldehyde overnight, and the cell adhesion and growth condition on the dermal scaffold of each sample were observed under laser scanning confocal microscopy (LSCM, Leica, SP8) after immunofluorescence staining with phalloidin-rhodamine and DAPI on the second day. The other part was successively dehydrated in a gradient of 50%, 70%, 90%, and 100% ethanol. Next, the sections were dried in a freeze-dryer, coated with a thin layer of gold, and prepared for SEM scanning.

In vivo study

Full-thickness skin defect model and experimental grouping. A total of six male Bama miniature pigs weighing approximately 20 kg were used in this study. The animals were kept in individual cages, and their body states were closely monitored. All animal procedures were performed in accordance with the Guidelines for Care and Use of Laboratory Animals of Guangdong Institute of Laboratory Animals, China, and approved by the Animal Ethics Committee of Guangdong Institute of Laboratory Animals, China.

The Bama miniature pigs were first sedated by intramuscular injection of chlorpromazine. Then, anesthesia was induced by intravenous injection of propofol and maintained by inhalation of isoflurane. After successful anesthesia, the back hair was removed. Two days later, the animals were anesthetized again in the same way. The skin was disinfected with 10% povidone-iodine solution, and four square full-thickness skin defects with sides of 5 cm were prepared 5 cm apart. The animals were divided into two groups: the experimental group (meshed ADS) and the control group (ADS). Next, each group was further divided into two subgroups, the negative pressure wound therapy (NPWT) group and the partial pressure bandage package (PBP) group, according to the scaffold fixation method. This experiment was an autologous and allogeneic controlled study, and each subgroup was repeated six times.

All wounds underwent a two-stage operation (the first stage was ADS transplantation, and the second stage was an autologous split-thickness skin graft). The specific experimental grouping is shown in Table 1, and each Bama miniature pig

Table 1 Specific experimental groups

Group	Sub-groups
Experimental group (meshed-ADS)	Group a (meshed-ADS + NPWT) Group b (meshed-ADS + PBP)
Control group (ADS)	Group c (ADS + NPWT) Group d (ADS + PBP)

ADS: artificial dermal scaffold; meshed-ADS: meshed artificial dermal scaffold; NPWT: negative pressure wound therapy; PBP: partial pressure bandage package.

and the full-thickness skin defect were numbered as shown in Fig. 1.

Operation procedure. Four full-thickness skin defects 5 cm × 5 cm in size were prepared on the back of each Bama miniature pig. Then, the wounds were treated in two steps, as follows. The wounds were first covered with ADSs or meshed ADSs, which were fixed with PBP or a negative pressure drainage device (Shenzhen Qikang Medical Equipment Co., Ltd, China) with a negative pressure value of 100–120 mmHg. Specific pressure bandages were applied to ensure efficient dressing. Afterward, each Bama miniature pig was kept in an individual cage; their body state was closely monitored, and the negative pressure device or PBP dressing was replaced regularly. The second step, an autologous split-thickness skin graft, was performed on day 10 (d10). The negative pressure device, PBP dressing, and upper silicone were carefully removed, and the wound substrates were thoroughly cleaned. Next, the corresponding size of autologous split-thickness skin, which was taken from the pig's own buttock and back, was transplanted to the wound, dressed with sterile gauze, and fixed with PBP. Finally, each pig was dressed with specific pressure bandages and kept in an individual cage to observe the indices described below. The operation process is shown in Fig. 2.

General observation. The oedema, exudate, or empyema of wounds; the dissolution, necrosis, and shedding of the ADS; and the granulation tissue coverage of the wounds were dynamically observed on d4, d7, d10, d14, d17, d21, d28, d60, and d90 following the first-stage operation. Images of wounds were collected at different points in time.

Take rate and contraction rate of grafted skin. The take rate of autologous split-thickness skin grafts was evaluated at d10 after the second-stage operation. Wound contraction was evaluated in the first month, the second month, and the third month fol-

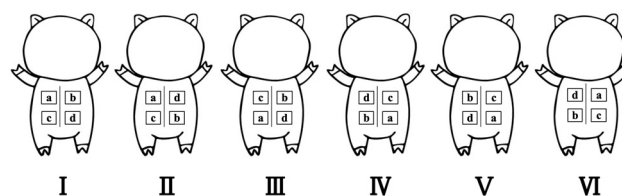


Fig. 1 Experimental numbering of Bama miniature pigs and full-thickness skin defects.



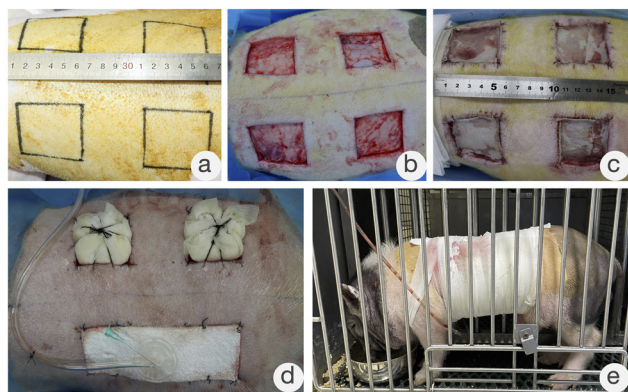


Fig. 2 The operation process. (a) Design of the wounds sized 5 cm \times 5 cm on the back of the Bama miniature pig. (b) Preparation of the full-thickness skin defects. (c) General view of wounds immediately after the autologous split-thickness skin graft. (d) Wound management after the first surgery according to the primary design (NPWT or PBP). (e) Postoperative feeding conditions.

lowing the first-stage operation. The specific calculation method is as follows. The wound was covered with a transparent film with grids (OPSITE FLEXIGRID, Smith & Nephew). The number of grids for each measured area was calculated, in which an area occupying more than half a grid was recorded as one grid, and an area occupying less than half a grid was ignored. The measuring area was calculated as the number of grids \times the area of each grid (1 cm²). The area of the current wound and postgraft skin were measured using this method. Both the original skin graft area and the original wound area were 5 cm \times 5 cm. Finally, the take rate of the skin graft was calculated as (the survival skin graft area/the original skin graft area) \times 100%. The wound contraction rate was calculated as (the original wound area – the current wound area)/the original wound area \times 100%.

Histological assessment. Bama miniature pigs were anesthetized using the method described above. The sampling method was as follows. After the pigs were anesthetized, two biopsy samples (3 mm in diameter) were taken by a skin sampler from the indicated position of the indicated wound in each subgroup at different time intervals. The designated sampling wound and position at different time intervals were based on the animal number and location of the wound.

CD31 staining was performed at d4, d7, d10, d14, d17, and d21 following the first-stage operation to evaluate dermal angiogenesis. In addition, HE staining was performed at d4, d7, d10, d14, d17, d21, d28, d60, and d90 following the first-stage operation to evaluate local inflammation, ingrowth of cells and tissues in the dermal scaffold, and *in vivo* degradation of the dermal scaffold. The specific experimental operation and histopathological detection means were the same as those reported in previous studies.²³

Statistical analysis

SPSS 19.0 software was utilized for statistical analysis, and the data were recorded as the mean \pm SD. The *t*-test for indepen-

dent samples was used for comparisons between two groups, and the χ^2 test was used to compare the proportions and proceed with correlation analysis of two or more groups. *p* < 0.05 indicated a significant difference.

Results

Characterization

Morphology. The microstructures of the meshed ADS and ADS were observed by SEM. The through-layer channels arranged in parallel longitudinal and transverse intersections 2 mm long and 1.5 mm apart were observed on the surface and underside of the meshed ADS, and the structure of the meshed ADS was observed without shrinkage or collapse (Fig. 3a–c). The double-layer structure of the ADS was observed on the cross-section view (Fig. 3f). Its upper layer was an intact smooth silicone membrane (Fig. 3d), and the lower layer was a cross-linked collagen–chondroitin sulfate dermal scaffold with a large number of homogeneous circular or ellipsoidal pores, with a pore size of 111 ± 46 μ m (Fig. 3e).

Physical properties. As shown in Fig. 4a, the porosity of the meshed ADS was $95.13 \pm 2.27\%$ and that of the ADS was $96.08 \pm 1.31\%$. There was no significant difference between them. In addition to porosity, the physical characteristics of tensile strength and *in vitro* degradation were measured. As shown in Fig. 4b, the maximum tensile strength of the meshed ADS was 3.05 ± 0.34 N, and that of the ADS was 8.07 ± 2.36 N. Compared with that of the ADS, the tensile strength of the meshed ADS decreased significantly (*p* < 0.05). The enzymatic degradation rates of the meshed ADS at 5 h, 10 h, and 24 h were $58.08 \pm 1.60\%$, $82.11 \pm 1.83\%$, and $93.84 \pm 4.56\%$, respectively, and those of the ADS were $51.87 \pm 6.90\%$, $75.09 \pm 6.03\%$, and $93.18 \pm 4.31\%$, respectively. There was no significant difference between the two at any time point (Fig. 4c).

Cytocompatibility

In this study, L929 cells and HUVECs were used for cytocompatibility tests. As shown in Fig. 5 and 6, the results of laser scanning confocal microscopy (LSCM) and scanning electron

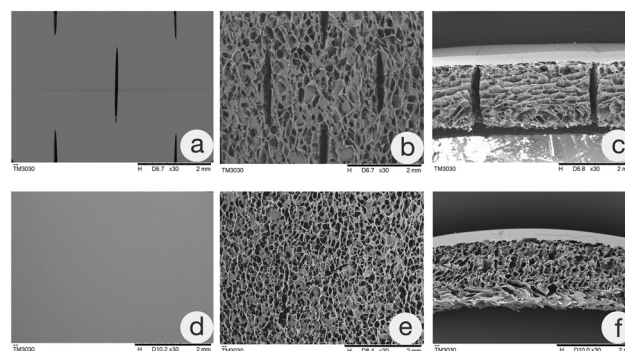


Fig. 3 The microstructure of the meshed ADS and ADS. (a–c) The surface, underside, and cross-section view of the meshed ADS. (d–f) The surface, underside, and cross-section view of the ADS.



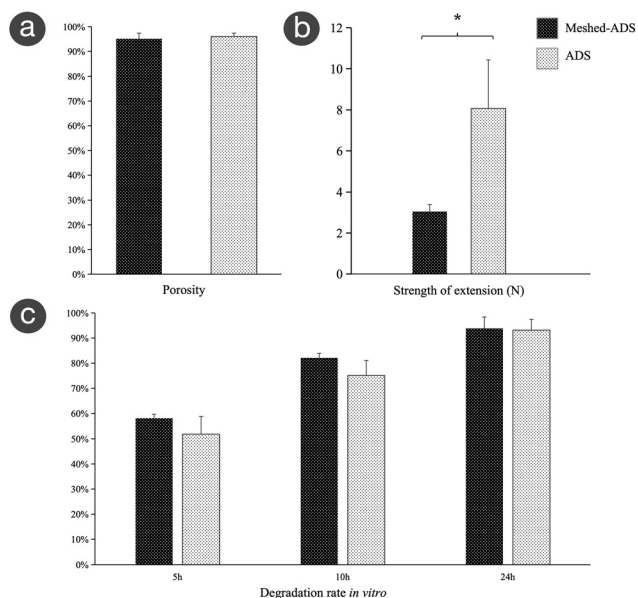


Fig. 4 Physical properties. (a) There was no significant difference in the porosity of the ADS and the meshed ADS. (b) The tensile strength of the meshed ADS was poorer than that of the ADS (* $p < 0.05$). (c) There was no significant difference in the enzymatic degradation rate of the ADS and meshed ADS at different time points.

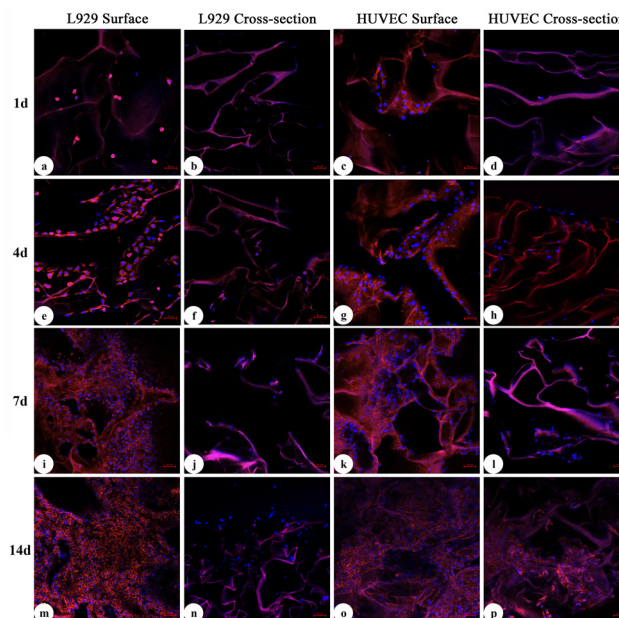


Fig. 6 LSCM images of cytocompatibility. (a, e, i, m) ($\times 300$) and (b, f, j, n) ($\times 1000$) Images of L929 adherence and proliferation conditions on the meshed ADS at d1, d4, d7 and d14 after coculture. (c, g, k, o) ($\times 300$) and (d, h, l, p) ($\times 1000$) Images of HUVECs adherence and proliferation conditions on the meshed ADS at d1, d4, d7 and d14 after coculture.

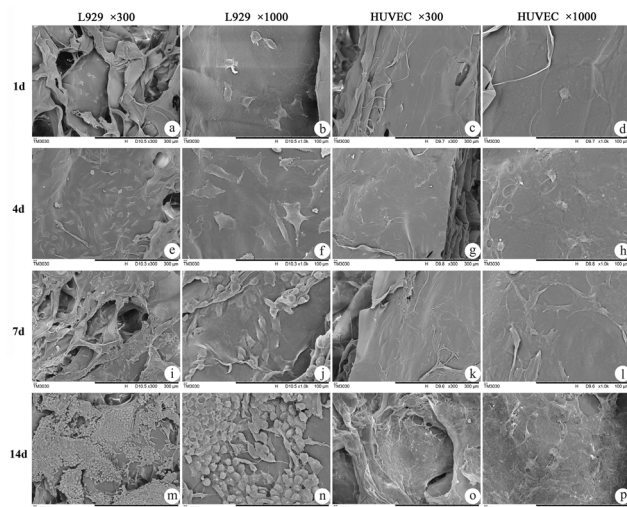


Fig. 5 SEM images of cytocompatibility. (a, e, i, m) ($\times 300$) and (b, f, j, n) ($\times 1000$) Images of L929 adherence and proliferation conditions on the meshed ADS at d1, d4, d7 and d14 after coculture. (c, g, k, o) ($\times 300$) and (d, h, l, p) ($\times 1000$) Images of HUVECs adherence and proliferation conditions on the meshed ADS at d1, d4, d7 and d14 after coculture.

microscopy (SEM) showed that at d1 after coculture, only scattered cells had begun to attach to the pore walls. At d4, the cells were firmly attached to the scaffold and began to proliferate rapidly. At d7, most of the cells had expanded. At d14, the cells had extended into sheets and grew inside along the scaffold, which exhibited sufficient adhesion and expansion of cells on the surface of the meshed ADS. According to these

results, we believed that due to its good affinity, as long as a small number of cells adhered to the surface of the meshed ADS, the cells could rapidly proliferate, extend, and migrate into its interior structure, which indicated that the meshed ADS had good biocompatibility and no adverse effects on the metabolic process of cells.

Evaluation *in vivo*

Wound healing and general observation. As shown in Table 1, two groups were set up: the experimental group (meshed ADS) and the control group (ADS). Then, each group was further divided into two subgroups: the negative-pressure wound therapy (NPWT) group and the partial pressure bandage package (PBP) group. Each subgroup was repeated six times, and a total of 24 wounds were included in the study. All wounds were treated with a two-stage operation.

The dynamic progression of wound healing is shown in Fig. 7. When the wound dressings were changed at d4 after the first-stage operation, the ruddy dermis could be seen through the silicone layer in all groups. When the negative pressure device or PBP was removed at d10 after the first-stage operation, in addition to the ruddy dermal scaffold of each wound in Group a, necrosis, dropsy, or empyema of the dermal scaffold presented on individual wounds in the other groups. Then, the upper silicone was carefully removed, and the wound substrate was thoroughly cleaned. A uniform distribution of granulation tissue on the dermal scaffold was clearly observed. Next, the corresponding size of split-thickness autologous skin was harvested for grafting on each wound and fixed by PBP.



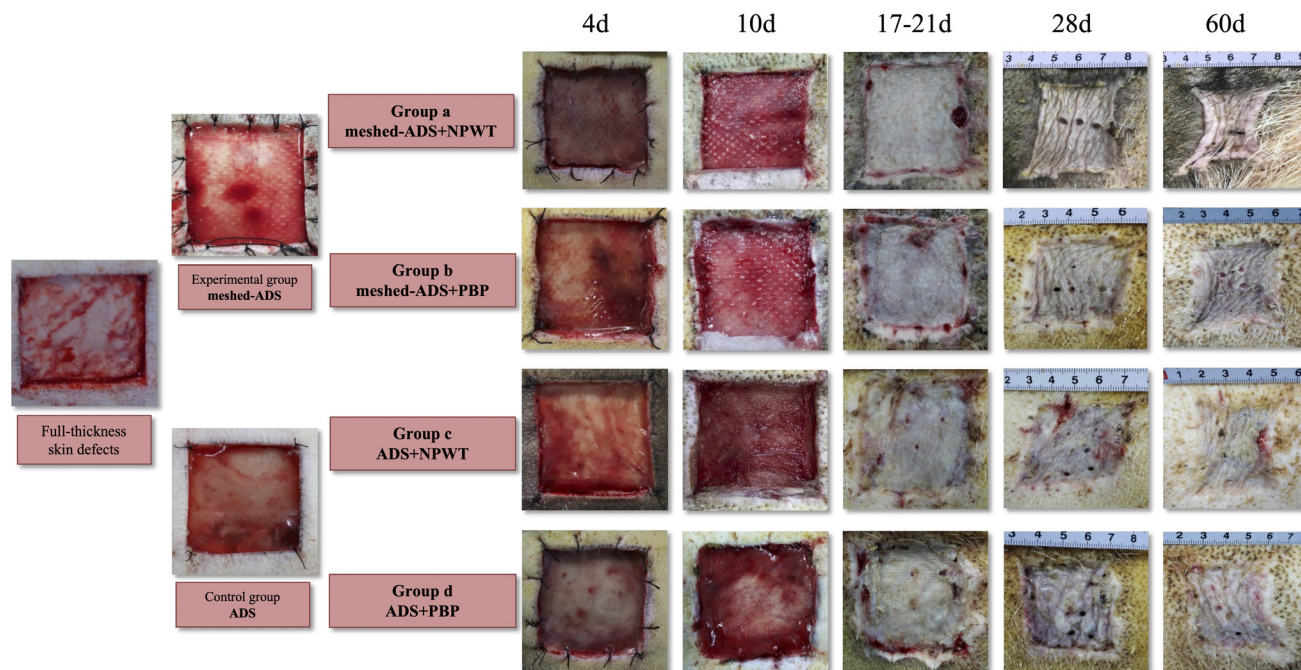


Fig. 7 General observations of the *in vivo* study. The dynamic progression of wound healing treated with meshed ADS + NPWT (Group a), meshed ADS + PBP (Group b), ADS + NPWT (Group c), and ADS + PBP (Group d) at d4, d10, d17–21, d28, and d60 after the first-stage operation.

The complications that occurred after the transplantation of the ADS or meshed ADS in Groups b, c, and d are shown in Fig. 8, including necrosis, dropsy, or empyema of the dermal scaffold (Fig. 8a and b), and the yellow-white appearance and partial liquefaction of the dermal scaffold (Fig. 8c). The image shown in Fig. 8d occurred in Group c, and the drainage pores (the red dashed line) were prepared immediately after hydrops and empyema of dermal scaffolds were detected. Next, the silicone layer was removed at d10 following the first-stage operation,

and the dermal scaffolds showed a ruddy appearance. All of the wounds with dermal-related complications underwent appropriate debridement to remove the necrotic and liquefied dermal scaffolds, and subsequently, autologous split-thickness skin grafts were performed.

Take rate and contraction of grafted skin. The graft skin take rate was evaluated at 7–11 d after the second-stage operation. The take rates of graft skin for Groups a–d were $92.33 \pm 2.50\%$, $87.67 \pm 6.44\%$, $85.67 \pm 7.87\%$, and $82.33 \pm 7.71\%$, respectively, which were greater than 80%, and each wound only retained a small unhealed area, as shown in Fig. 9a.

The contraction of grafted skin in each group was estimated at d28, d60, and d90 after the first-stage operation (Fig. 9b). The contraction rates of grafted skin for each group at the three time points were as follows. Group a: $48 \pm 7.56\%$, $56 \pm 8.66\%$, and $58 \pm 5.89\%$; Group b: $46 \pm 6.52\%$, $56 \pm 3.74\%$, and $62 \pm 8.40\%$; Group c: $49 \pm 7.69\%$, $61 \pm 6.55\%$, and $61 \pm 3.74\%$; and Group d: $46 \pm 4.46\%$, $54 \pm 5.39\%$, and $62 \pm 4.04\%$. Over time, there were no significant differences among the four groups ($p > 0.05$), and the contraction rates of the experimental group and control group showed an increasing trend and tended to be stable.

Inflammation and histocompatibility *in vivo*. As shown in Fig. 10, at d4 after the first-stage operation, cells grew into the dermal scaffold from the junction of the dermal scaffold and the wound (Fig. 10a–d). At d7 (Fig. 10a–d), more cells could be seen on the dermal scaffolds. At d10 (Fig. 10e–h), many myofibroblasts, fibroblasts, and endothelial cells grew into the dermal scaffold from the junction of the dermal scaffold and the wound. In addition, a small number of inflammatory cells,

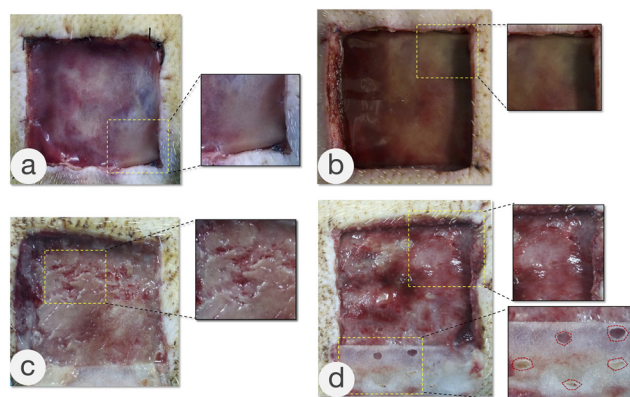


Fig. 8 Complications after the transplantation of the ADS or meshed ADS. (a and b) Necrosis, dropsy, or empyema of the dermal scaffold. (c) Yellow-white appearance and partial liquefaction of the dermal scaffold after silicone layer removal. (d) Drainage pores (the red dashed line) were prepared immediately after the detection of hydrops or empyema. At d10 after silicone layer removal, the dermal scaffolds showed a satisfactory ruddy appearance.



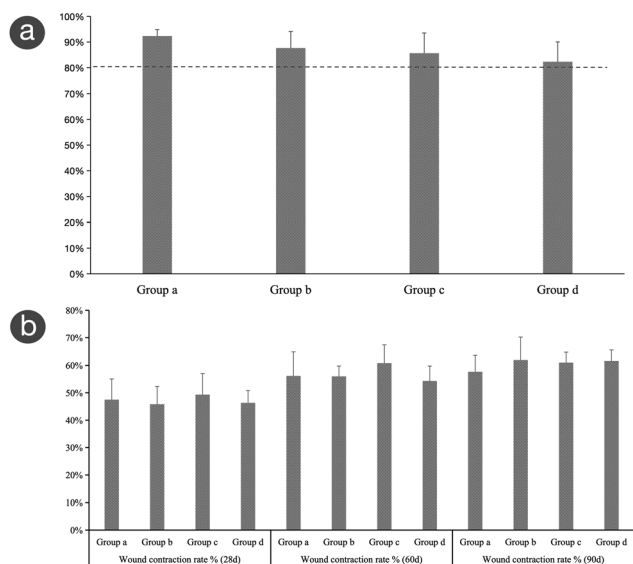


Fig. 9 Take rate and contraction of grafted skin. (a) There was no significant difference in the take rate of grafted skin among the different groups at d7–11 after the second-stage operation. (b) There was no significant difference in the contraction rate of grafted skin for each group at d28, d60, and d90 after the first-stage operation.

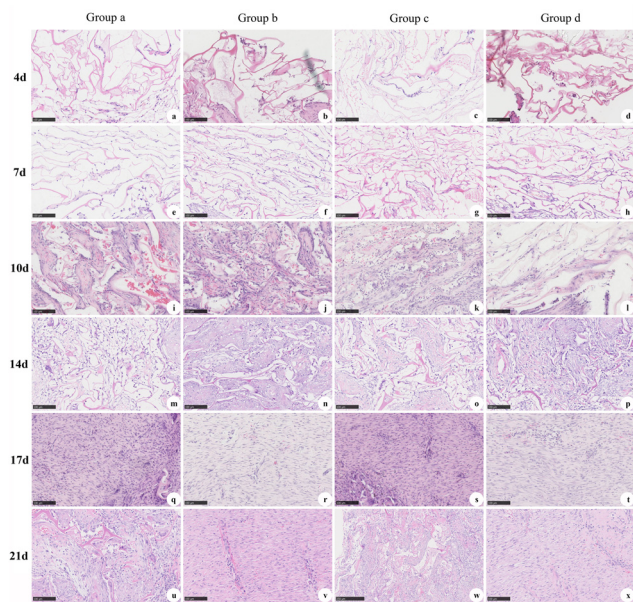


Fig. 10 Inflammation and histocompatibility *in vivo*. Dynamic changes in the dermal scaffold and inflammation in the four groups (Group a–d) at d4 (a–d), d7 (e–h), d10 (i–l), d14 (m–p), d17 (q–t) and d21 (u–x) after the first-stage operation.

mainly monocytes, and a small number of lymphocytes, multinucleated cells, and eosinophils were observed in the dermal scaffold. At d14 and d17, many myofibroblasts, fibroblasts, and endothelial cells grew into the dermal scaffold, regenerative tissue was distributed throughout the dermal scaffold, and the number of inflammatory cells was gradually reduced (Fig. 10m–t). At d21, except for a small number of multinucleated cells

around the residual dermal scaffold, the inflammation disappeared (Fig. 10u–x). In addition, many regenerating fibers filled the whole dermal scaffold with a dense distribution, and the residual collagen fibers of the ADS were disordered and dispersed. An obvious vascular network was established between the graft skin and vascularized dermal scaffolds, and there were no significant differences in the inflammatory response and cell proliferation among all groups at each time point.

The results of HE staining of the experimental groups and control groups at d28, d60, and d90 after the first-stage operation are shown in Fig. 11. At 28 d, proliferation of the fibrous structure was observed (Fig. 11a–d). At d60, the regenerative tissue was nearly mature (Fig. 11e–h). At d90, the collagen fibers of the regenerative tissue were arranged in bundles and interlaced with each other, some of which were close to the normal tissue (Fig. 11i–l).

Degradation *in vivo*. As shown in Fig. 10, within the first four weeks after the first-stage operation, the outline of the dermal scaffolds was clear, and the original morphology was still maintained. Then, with the continuous ingrowth of cells and regenerative tissues, the scaffold disintegrated gradually. More than three to four weeks after the first-stage operation, dermal scaffolds had degraded gradually; a small number of scaffolds remained on some wounds, and the tissue reaction tended to be stable (Fig. 11a–d). Two-to-three months after the first-stage operation, a small number of dermal scaffolds could be seen on each wound, and the tissue reaction was stable (Fig. 11e–i). There was no significant difference in dermal scaffold degradation *in vivo* among the different groups, which was consistent with the results of tissue ingrowth.

Dermal angiogenesis *in vivo*. As shown in Fig. 12, immunohistochemistry staining of CD31 represented the artificial dermal angiogenesis of the experimental groups and control groups at different time points. At d4, d7, and d10 after the first-stage operation, the number of new vessels in the dermal scaffold of different groups increased successively (red arrows indicate the neoangiogenesis lumen), which indicated that the proliferation, expansion, and neoangiogenesis of endothelial cells in the scaffolds required a certain period (Fig. 12a–h). At d10 and d14, the new vessels were gradually distributed throughout the whole dermal scaffold (Fig. 12i–p). At d17 and

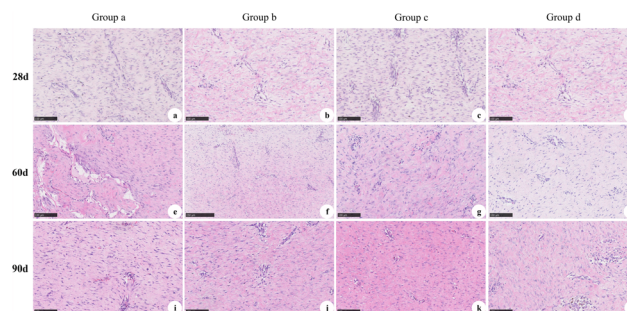


Fig. 11 Long-term degradation *in vivo*. Dynamic degradation of the dermal scaffolds of the four groups (Group a–d) at d28 (a–d), d60 (e–h) and d90 (i–l) after the first-stage operation.



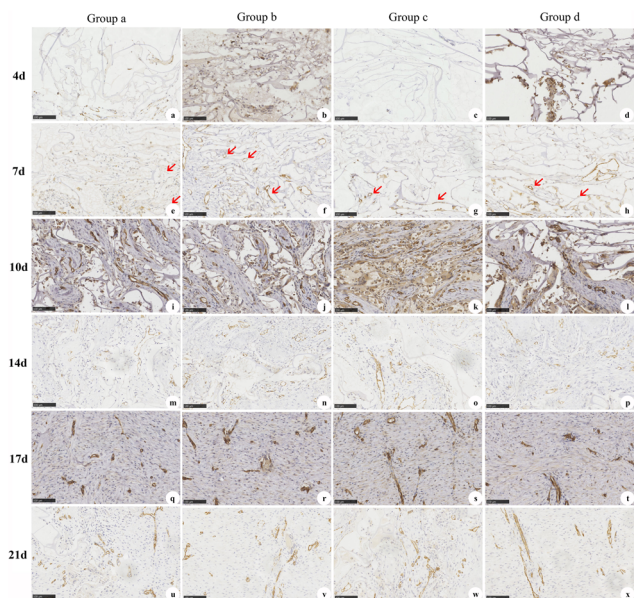


Fig. 12 Dermal angiogenesis *in vivo*. Dynamic angiogenesis of the dermal scaffolds of the four groups (Group a–d) at d4 (a–d), d7 (e–h), d10 (i–l), d14 (m–p), d17 (q–t) and d21 (u–x) after the first-stage operation.

d21, the neoangiogenesis and tissue structure tended to be mature, forming a complete skin structure (Fig. 12q–x). There was no significant difference in artificial dermal angiogenesis among all groups.

Discussion

Although the emergence of the ADS provides a new option for the treatment of deep wounds, problems such as unsatisfactory dermal angiogenesis, inadequate drainage, local dropsy, and even empyema should not be ignored.^{24,25} Therefore, to improve its clinical effects, the focus of ADS development has been optimizing dermal angiogenesis and self-drainage by altering its composition and structure or combining it with other therapeutic means.^{15,26}

The mesh technique is a technical method of improving the biological function of the ADS by modifying its physical structure. That is, a specific mesh machine is used to prepare channels throughout the whole layer that are regularly arranged in parallel longitudinal and transverse intersections in a specific proportion to enhance its longitudinal drainage, preventing the formation of local dropsy or empyema.²⁷ In addition, the meshed ADS exhibits increased compliance, which makes it suitable for wounds in nearly any location.²⁸ In breast reconstruction, meshed ADSs could reduce the incidence of postoperative infection, hematoma, and seroma and shorten the drainage time.⁸ In addition, the meshed ADS is potentially cost-effective because it scales up the ADS surface and improves its actual coverage.²⁹ In this study, the meshed ADS was prepared in a specific proportion and without shrinkage or collapse. SEM showed that the meshed ADS had a

regular staggered mesh throughout the whole layer. Further research confirmed that, except for the decreased tensile strength, the meshed ADS had no significant differences from the ADS in porosity or degradation. Cell coculture and *in vivo* experiments confirmed that both ADSs had good cytocompatibility and histocompatibility. Therefore, the meshed ADS prepared in this study still maintains superior physicochemical properties, which can meet the needs of *in vivo* research and clinical application.

Angiogenesis is one of the major issues in tissue regeneration and repair and is indispensable for satisfactory wound repair by delivering oxygen and nutrients to reparative cells located around the wound. However, the dermal angiogenesis of ADS is barely satisfactory. Methods to improve dermal angiogenesis have always been a topic of interest.³⁰ Currently, the strategies mainly include three-dimensional bioprinting,^{31,32} the transplantation of angiogenesis-related genes,³³ the implantation of prefabricated vascular scaffolds,^{34,35} and the modification of structure and physicochemical properties.¹⁵ In this study, we modified the physical structure of the ADS to have a meshed appearance. This unique structure can enhance the drainage of the ADS and decrease the risk of local dropsy or empyema.²⁸ In addition, due to the increased longitudinal mechanical stress, it may improve the angiogenesis of endothelial cells and accelerate the formation of the vascular network.¹⁹ However, the results of this study confirmed that although the meshed ADS possessed stronger longitudinal mechanical stress, there was no significant difference in dermal angiogenesis. Surprisingly, the regenerative tissue had slightly different growth patterns in the meshed ADS due to the presence of the mesh structure. The mesh structure made it easier for cells and extracellular matrix to grow vertically and horizontally into the dermal scaffolds, which is more favorable to achieving complete angiogenesis.

In addition to improving self-structure, ADS combined with NPWT is a novel method to enhance dermal angiogenesis.^{36,37} NPWT is a commercial approach to managing complex acute and chronic wounds that can provide a favorable wound microenvironment to improve wound repair.^{16,38} NPWT can not only increase the number of microvascular structures in the early stage of wound repair but also promote the stability and maturation of microvascular structures in the later stage, thus affecting local blood perfusion.¹⁸ In this study, although meshed ADS and ADS combined with NPWT had better dermal angiogenesis than PBP, the difference was not statistically significant. However, the inflammation in the NPWT group was relatively mild during the entire treatment process, which may be closely related to its closed and low oxygen environment, thus ensuring angiogenesis stimulation, thorough drainage, and low infection incidence.^{39,40}

In addition to angiogenesis, local infection is another vital problem caused by poor drainage, which may lead to local necrosis, dropsy, or empyema. In this study, it was observed that whether combined with NPWT or PBP, ADS showed local necrosis, dropsy, or empyema, with an incidence of 3/24. Even if local drainage pores were operated on in time, dermal angio-



genesis was still greatly affected, thus delaying wound repair. During the widespread communication with peers about the application of ADS, we found that most clinicians encounter the same problems. Therefore, in routine clinical practice, regardless of whether the ADS is used alone or combined with other therapeutic means, it is likely that drainage pores or manual fenestration to increase the drainage efficiency beforehand will be necessary. In addition, there was still a certain incidence of dermal dropsy or empyema, which tended to result in delayed wound healing or even reoperation. In this study, we found that one wound in Group b, the meshed ADS + PBP group, presented obvious dropsy and empyema with a yellow-white appearance. However, in the meshed ADS + NPWT group, the dermal scaffold showed good performance without any adverse reactions and demonstrated a better survival rate of grafted skin and wound healing. Therefore, we believe that adequate negative pressure drainage and a specific mesh structure can accelerate the clinical effects of ADSs.

Therefore, the results of this study demonstrated that the mesh structure does not affect the physicochemical properties of the ADS. Because of the mesh structure, the meshed ADS likely facilitates drainage of the exudate and reduces the risk of dropsy or empyema, which may guarantee satisfactory dermal angiogenesis. At the same time, a meshed ADS with a flexible and soft structure combined with NPWT can ensure better adhesion to the wound surface and complete drainage, especially for wounds located in unique positions or suffering from dropsy and dermal chronic ulcers. The ADS used in this study has already been commercialized, and the major physicochemical properties of the meshed ADS were not changed with the addition of the mesh structure. The prepared meshes were uniform, with no inconsistencies caused by different physicians.

As a preliminary exploratory study on a method to improve the clinical effects of ADSs, the design and implementation of this study need to be further improved. NPWT treatment includes continuous, intermittent, and dynamic negative pressure models. It has been reported that among the three models, dynamic negative pressure was more conducive to inducing granulation tissue hyperplasia and angiogenesis.⁴¹ Negative pressure values of NPWT that are too low may not achieve the proper mechanical stress, and values that are too high will overcompress the three-dimensional structure of the ADS, neither of which is conducive to guiding the dermal regeneration and angiogenesis processes. In this study, the working model of NPWT was continuous, and the pressure value was 100–120 mmHg, which is considered appropriate at present.⁴² No other working models were used in this study, which might affect the research reliability and validity, and they should be further investigated.

Our clinical work showed that the wound contraction would occur after skin graft and generally tended to be stable after 3 months. The results of this research also confirmed that the wound contraction rate tended to be stable 2–3 months post-surgery, which was consistent with the results reported in the literature.⁴³ Thus, we planned the 3 months post-surgery as the observation endpoint in this research. A longer research

period may be planned for our future work. Another limitation of our study was the lack of surgical scar assessment, such as the Vancouver Scar Scale (VSS) and durometer and cutometer evaluation,⁴⁴ which would help to support the research conclusions. These scar assessments would certainly be carried out in our future work. According to the current findings, we believe that the meshed ADS prepared in this study has better compliance and is suitable for various types of wounds and wound sites. A meshed ADS combined with NPWT was more easily fixed on the wound site and was more conducive to wound drainage, avoiding the occurrence of local dropsy or empyema, which has great potential to be a better wound management method in the treatment of various wounds.

Conclusions

The meshed ADS prepared in this study had a regular staggered through-layer mesh and possessed stable physicochemical properties and good biocompatibility. Compared with other groups, a meshed ADS combined with NPWT can ensure adequate subdermal drainage and reduce the risk of local dropsy or empyema, improving the quality and efficiency of wound repair, which can help physicians implement effective wound management.

Author contributions

The research was conceptualized by ZR.X. and ZH.C. and investigated by P.W., L.J.W., and HT.X. The data were analyzed by RW.T. The initial draft of the manuscript was written by P. W. and L.J.W. and was reviewed and edited by all contributing authors.

Conflicts of interest

There are no conflicts to declare.

Acknowledgements

This work was supported by the High-level Hospital and Clinical Specialty Discipline Construction Programme for Fujian Medical Development, China ([2021]76), the Fujian Provincial Key Laboratory of Burn and Trauma, the National Natural Science Foundation of China (82002034), and the Joint Funds for the Innovation of Science and Technology, Fujian Province, China (2021Y9068).

References

- 1 V. Dill and M. Morgelin, *Int. Wound J.*, 2020, **17**, 618–630.
- 2 R. Simman and L. Phavixay, *The Journal of the American College of Clinical Wound Specialists*, 2011, **3**, 55–59.



- 3 P. A. Hudgins, *Eur. J. Radiol.*, 2002, **44**, 130–138.
- 4 E. Lucich, J. Rendon and I. Valerio, *Regener. Med.*, 2018, **13**, 443–456.
- 5 F. D. Francesco, A. Busato, S. Mannucci, N. Zingaretti, G. Cottone, F. Amendola, M. D. Francesco, F. Merigo, V. Riccio, L. Vaienti, P. C. Parodi, A. Sbarbati and M. Riccio, *J. Int. Med. Res.*, 2020, **48**, 1–22.
- 6 B. D. Angelis, F. Orlandi, M. F. L. M. D'Autilio, M. G. Scioli, A. Orlandi, V. Cervelli and P. Gentile, *Int. Wound J.*, 2018, **15**, 1–12.
- 7 B. De Angelis, F. Orlandi, M. F. L. Morais D'Autilio, C. Di Segni, M. G. Scioli, A. Orlandi, V. Cervelli and P. Gentile, *J. Clin. Med.*, 2019, **8**, 525.
- 8 M. Schefflan, H. Grinberg-Rashi and K. Hod, *Plast. Reconstr. Surg.*, 2018, **141**, 1e–10e.
- 9 C. Z. Koyuncuoglu, S. Metin, I. Saylan, K. CaliSir, O. Tuncer and A. Kantarci, *J. Oral Implantol.*, 2014, **40**, 714–721.
- 10 S. Berg, K. Andresen and J. Rosenberg, *Surg. Innov.*, 2017, **24**, 289–298.
- 11 R. L. Pollard, P. J. Kennedy and P. K. Maitz, *J. Plast. Reconstr. Aesthet. Surg.*, 2008, **61**, 319–322.
- 12 N. S. Moiemmen, E. Vlachou, J. J. Staiano, Y. Thawy and J. D. Frame, *Plast. Reconstr. Surg.*, 2006, **117**, 160–174.
- 13 A. W. Chua, Y. C. Khoo, B. K. Tan, K. C. Tan, C. L. Foo and S. J. Chong, *Burns Trauma*, 2016, **4**, 3.
- 14 P. Lohana, S. Hassan and S. B. Weston, *Ann. Burns Fire Disasters*, 2014, **27**, 17–21.
- 15 F. S. Frueh, M. D. Menger, N. Lindenblatt, P. Giovanoli and M. W. Laschke, *Crit. Rev. Biotechnol.*, 2017, **37**, 613–625.
- 16 B. Dongmei Ge, *Adv. Skin Wound Care*, 2018, **3**, 421–428.
- 17 C. Huang, T. Leavitt, L. R. Bayer and D. P. Orgill, *Curr. Probl. Surg.*, 2014, **51**, 301–331.
- 18 G. E. Glass, G. F. Murphy, A. Esmaeili, L. M. Lai and J. Nanchahal, *Br. J. Surg.*, 2014, **101**, 1627–1636.
- 19 D. Stiefel, C. M. Schiestl and M. Meuli, *J. Pediatr. Surg.*, 2009, **44**, 575–580.
- 20 M. Leffler, R. E. Horch, A. Dragu and A. D. Bach, *J. Plast. Reconstr. Aesthet. Surg.*, 2010, **63**, e32–e35.
- 21 H. W. Shao, X. G. Wang, Z. G. You and C. M. Han, *Zhonghua Shaoshang Zazhi*, 2017, **33**, 523–525.
- 22 N. S. Moiemmen, J. Yarrow, D. Kamel, D. Kearns and D. Mendonca, *Burns*, 2010, **36**, 764–768.
- 23 Z. Xu, X. Chen, R. Tan, Z. She, Z. Chen and Z. Xia, *Mater. Sci. Eng., C*, 2019, **105**, 110063.
- 24 F. S. Frueh, M. D. Menger, N. Lindenblatt, P. Giovanoli and M. W. Laschke, *Crit. Rev. Biotechnol.*, 2017, **37**, 613–625.
- 25 L. Bargues, S. Boyer, T. Leclerc, P. Duhamel and E. Bey, *Ann. Chir. Plast. Esthet.*, 2009, **54**, 533–539.
- 26 L. Zhang, T. Weng, P. Wu, Q. Li, C. Han and X. Wang, *BioMed Res. Int.*, 2020, **2020**, 8824737.
- 27 E. R. Pope, *Vet. Clin. North Am. Small Anim. Pract.*, 1990, **20**, 177–187.
- 28 N. Zingaretti, G. F. Guarneri, F. De Biasio, M. A. Shoeib and P. C. Parodi, *Aesthetic Plast. Surg.*, 2018, **42**, 1704–1706.
- 29 A. Maisel Lotan, D. Ben Yehuda, T. M. Allweis and M. Schefflan, *Plast. Reconstr. Surg.*, 2019, **144**, 1045–1053.
- 30 A. Weisel, R. Cohen, J. A. Spector and Y. Sapir-Lekhovitser, *J. Tissue Eng. Regener. Med.*, 2022, **16**, 1173–1183.
- 31 A. Mir, E. Lee, W. Shih, S. Koljaka, A. Wang, C. Jorgensen, R. Hurr, A. Dave, K. Sudheendra and N. Hibino, *Bioengineering*, 2023, **10**, 606–124.
- 32 C. Mandrycky, Z. Wang, K. Kim and D. H. Kim, *Biotechnol. Adv.*, 2016, **34**, 422–434.
- 33 R. Guo, S. Xu, L. Ma, A. Huang and C. Gao, *Biomaterials*, 2011, **32**, 1019–1031.
- 34 M. W. Laschke and M. D. Menger, *Biotechnol. Adv.*, 2016, **34**, 112–121.
- 35 J. Chen, D. Zhang, L. Wu and M. Zhao, *Polymers*, 2023, **15**, 2015.
- 36 Y. F. Diehm, S. Fischer, E. Gazyakan, G. Hundeshagen, D. Kotsougiani-Fischer, F. Falkner, U. Kneser and C. Hirche, *J. Plast. Reconstr. Aesthet. Surg.*, 2021, **74**, 357–363.
- 37 M. G. Jeschke, C. Rose, P. Angele, B. Fuchtmeyer, M. N. Nerlich and U. Bolder, *Plast. Reconstr. Surg.*, 2004, **113**, 525–530.
- 38 C. R. Maguire, R. Livingston, G. E. Phillips and R. M. Kimble, *Pediatr. Surg. Int.*, 2017, **33**, 823–827.
- 39 V. Pappalardo, F. Frattini, V. Ardita and S. Rausei, *Surg. Technol. Int.*, 2019, **34**, 56–57.
- 40 S. U. Eisenhardt, Y. Schmidt, J. R. Thiele, N. Iblher, V. Penna, N. Torio-Padron, G. B. Stark and H. Bannasch, *J. Plast. Reconstr. Aesthet. Surg.*, 2012, **65**, 640–649.
- 41 C. Baldwin, M. Potter, E. Clayton, L. Irvine and J. Dye, *Ann. Plast. Surg.*, 2009, **62**, 92–96.
- 42 L. C. Argenta and M. J. Morykwas, *Ann. Plast. Surg.*, 1997, **38**, 563–576.
- 43 F. B. Corrêa, J. C. D. Castro, I. R. Almeida, J. A. Farina-Junior and P. S. Coltro, *Wound Repair Regen.*, 2022, **30**, 222–231.
- 44 I. R. Almeida, A. C. Gonçaves, F. B. Corrêa, J. C. D. Castro, E. C. O. Guirro, J. A. Junior. Farina and P. S. Coltro, *Ann. Surg.*, 2023, **277**, 198–205.

